Proceedings World Geothermal Congress 2020+1
Reykjavik, Iceland, April - October 2021

Induced Seismicity and Deformation at Geothermal Fields in California, USA

Andrew J Barbour

United States Geological Survey, 345 Middlefield Rd, Menlo Park, Calif. USA 94025

abarbour@usgs.gov

Keywords: Induced Seismicity, Ground Deformation, Seismic Hazard, Geodesy, Seismology, California

ABSTRACT

Understanding natural and anthropogenic sources of strain accumulation and release is critical to the accuracy of hazard assessments at geothermal fields. While the genesis of naturally occurring seismic and geologic hazard potential lies in the balance between gravitational forces, tectonic loading and natural faulting, induced earthquakes and ground deformation are generally understood to be related to reservoir depletion. With the current state-of-the-art in geodesy and seismology, these phenomena can be measured with unprecedented spatial and temporal coverage, illuminating the inherent feedback between production and reinjection, dominant modes of moment release, permeability, and structural complexity. Here I draw comparisons between large, active geothermal fields in California (USA), namely Coso, Salton Sea, North Brawley, and Heber. Seismic and geodetic data collected at the fields, spanning decades, show that steady and time-varying geologic hazards (i.e., earthquakes and ground deformation) are common observations.

1. INTRODUCTION

In 2018, nearly 1/3 of the total energy generation in California was from renewable energy resources (CEC, 2019). Of that, about 15% (~13 TWh) came from geothermal power plants. The geothermal budget is dominated by a few fields, with the largest net contribution coming from The Geysers in Northern California (Figure 1). Additional significant contributions come from the Coso field in Central California and in Southern California, namely from Salton Sea, North Brawley, and Heber.

Geothermal fields tend to be located in high strain-rate and seismicity-rate regions (e.g., extensional tectonics), but elevated rates of deformation and induced seismicity are often linked to industrial activities since fluid-mass deficits are common byproducts of the industrial process of extracting energy: there is often less fluid volume available for reinjection than the volume of fluids produced except, theoretically, in the case of binary power generation (Axelsson, 2012).

Natural geothermal systems have been exploited as sources of renewable energy for decades. Without rapid groundwater recharge, the reservoir responds to fluid mass and temperature losses with volumetric contraction at depth: this drives subsidence, creates new faults and fractures, and pushes preexisting faults towards reactivation. Deformation induced by fluid-mass depletion (e.g., Segall, 1985) is likely to vary in both time (even if production is approximately constant) and space (Figure 2), and can dominate thermal effects in certain conditions (e.g., Segall and Fitzgerald, 1998).

Induced seismicity and ground deformation at geothermal fields in California have been documented extensively, especially at Coso and The Geysers. At The Geysers, injection and production rates drive deformation and promote stress changes that induce seismic moment release (Majer and Peterson, 2007; Mossop and Segall, 1997). Changes in faulting style have been linked to variations in injection and production rates (Martínez-Garzón, et al., 2016), suggesting feedback(s) between industrial activities (e.g., injection), changes in the state of stress and hydraulic permeability in the reservoir. The same feedbacks for the southern Californian fields have not been established with the same fidelity; hence, in this presentation I focus on observations from those fields.

2. OBSERVATIONS AND DISCUSION

The observations presented here for Coso, Salton Sea, North Brawley and Heber, include seismic and geodetic data. Seismic data include basic catalog locations and magnitudes from regional seismic networks; at Heber we also show earthquake catalogs from advanced event-detection techniques. Geodetic data include complementary data from space-borne methods and traditional ground-based leveling surveys.

2.1 Coso Geothermal Field

The Coso Geothermal Field (CGF), in Central California, has been in operation since the late 1980's. Some of the earliest studies using interferometric synthetic aperture radar (InSAR) at CGF (Fialko and Simons, 2000; Wicks, et al., 2001; Vasco, et al., 2002) suggested subsidence rates of nearly 35 mm/year, imaging the reservoir to be at approximately 2.5 km. Induced seismicity is documented with high-precision earthquake relocations (e.g., Kaven, et al., 2015) that reveal a dense network of faults and fractures that form the reservoir.

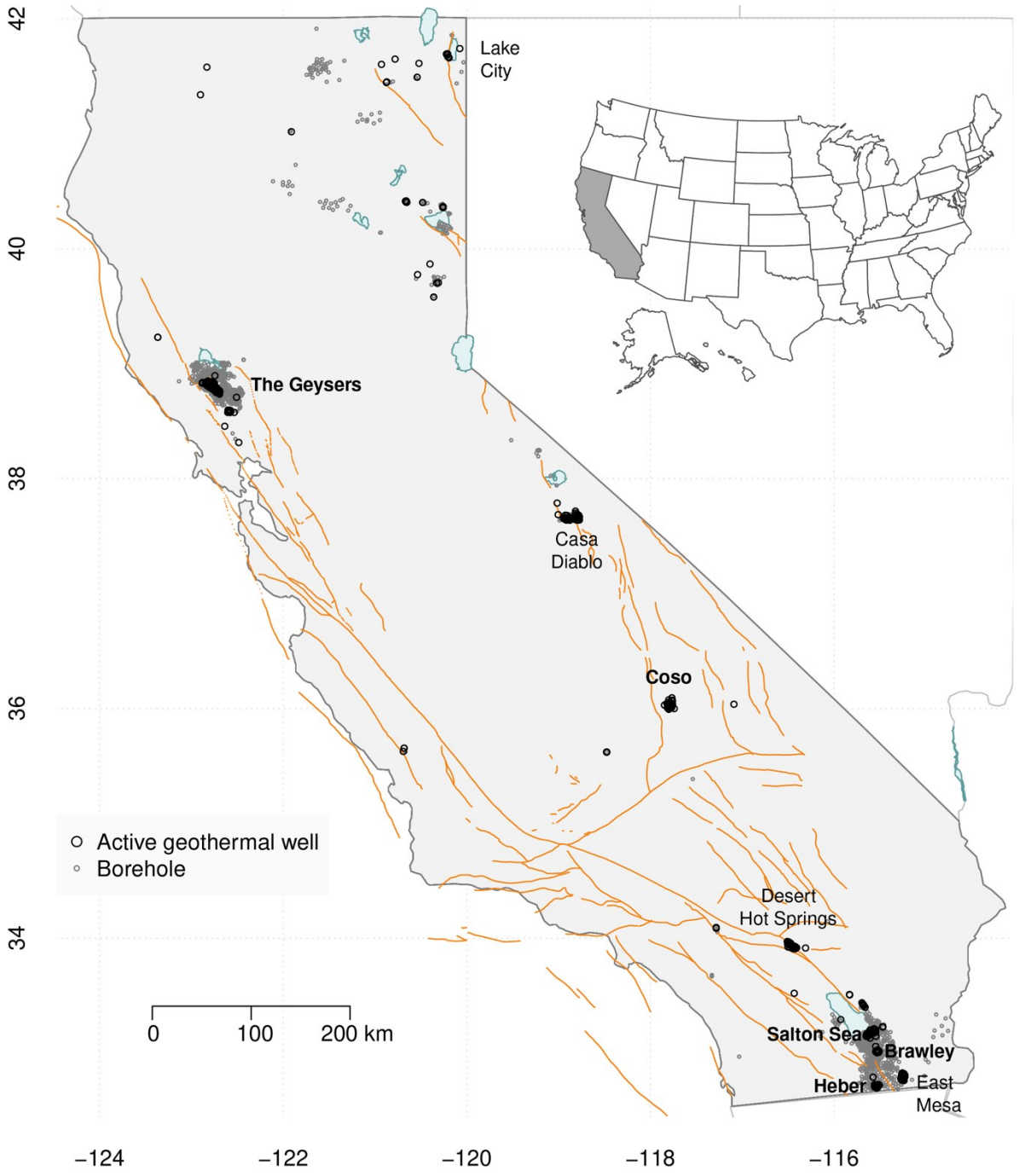

Figure 1: Geothermal wells and major faults in California. Grey circles denote all types of boreholes and dark circles mark active geothermal wells. The largest active fields are labeled, and the fields discussed in this paper are in bold. The inset map shows where California is located within the United States of America.

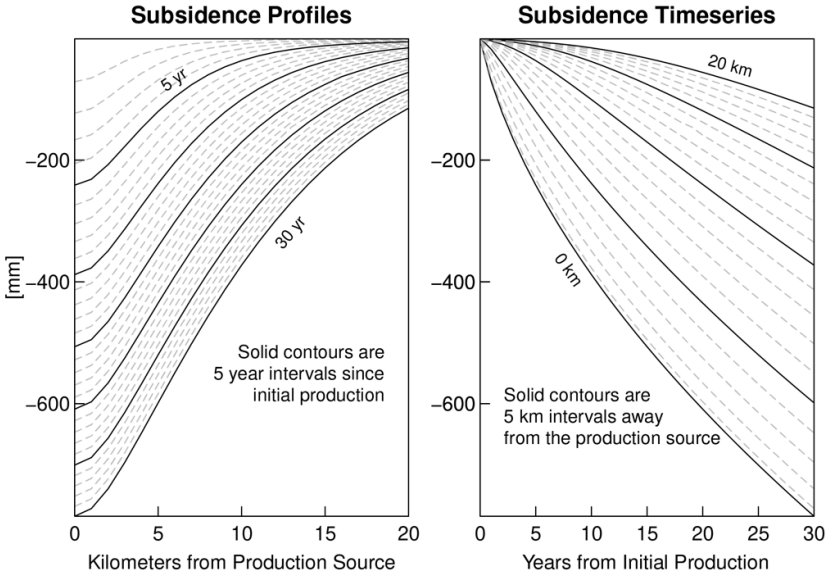

Figure 2: Poroelastic model of surface displacements associated with fluid withdrawal (Segall, 1985). These calculations assume a fluid-mass production rate of 20 Mt/yr from a reservoir at 2 km depth, with an undrained Poisson's ratio of 0.33, a Skempton's coefficient of 0.6, and a hydraulic diffusivity of 0.1 m^2/s. On the left: displacements as a function of distance from the source, with contours showing five-year intervals. On the right: surface displacements as a function of time, assuming a constant production rate; contours show five-kilometer distance intervals.

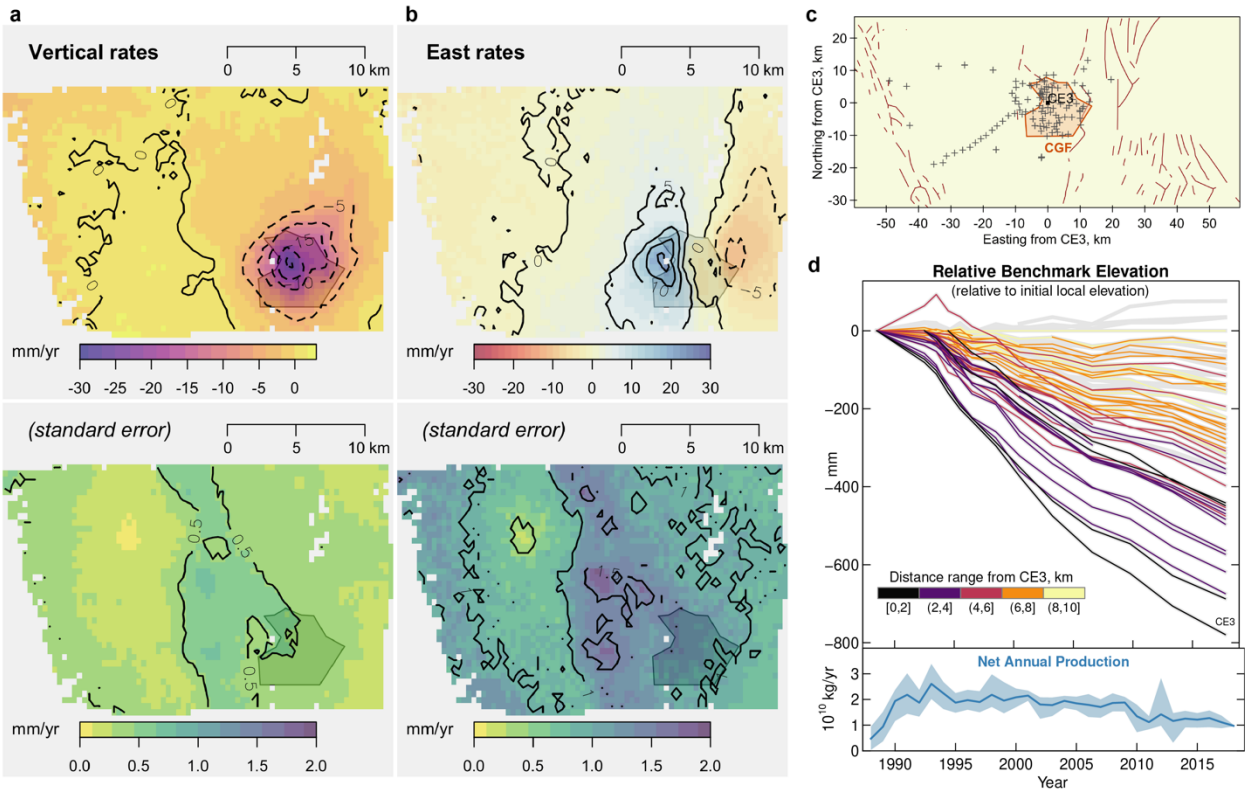

Figure 3: Observations of surface deformation at the Coso Geothermal Field (CGF – the shaded polygon) from InSAR (a – b) and leveling (c – d). Maps in (a) and (b) are vertical and east rates (in mm/yr; negative values represent subsidence or westward motion) from Envisat and Sentinel using permanent and distributed scatterers, PS and DS InSAR (Eneva, et al., 2018). The map in (c) shows the locations of leveling benchmarks at CGF, and the timeseries in (d) shows their relative positions as a function of time adapted from Eneva, et al., (2018), with colors representing radial distance from benchmark "CE3" – the benchmark showing maximum subsidence rates. Below that shows the net-annual production across the field, which has averaged between 15-20 Mt/yr since the late 1980's and declined some in the last decade.

Since the early InSAR studies listed above, the technology associated with InSAR processing has made considerable advancements. Recent work (Ali, et al., 2016; Eneva, et al., 2019) offer a much denser image of ground deformation at CGF, with timeseries that have been validated against traditional leveling surveys (Figure 3).

The spatial and temporal characteristics of these data closely match the expected motions from a simplified model of a contractional volumetric strain source embedded in a uniform, poroelastic halfspace (Figure 2). After fitting data from Coso with such a model, the optimal set of properties for the hypothetical depleting reservoir and the hydraulic diffusivity of the medium are in close agreement with previous work characterizing the geothermal system and local-to-regional scale patterns in seismicity (e.g., Chen and Shearer, 2012). However, because we lack data prior to the development of CGF, the preexisting feedback between permeability and moment release – seismic or otherwise – may be largely inseparable from the changes induced by anthropogenic production of the geothermal resource.

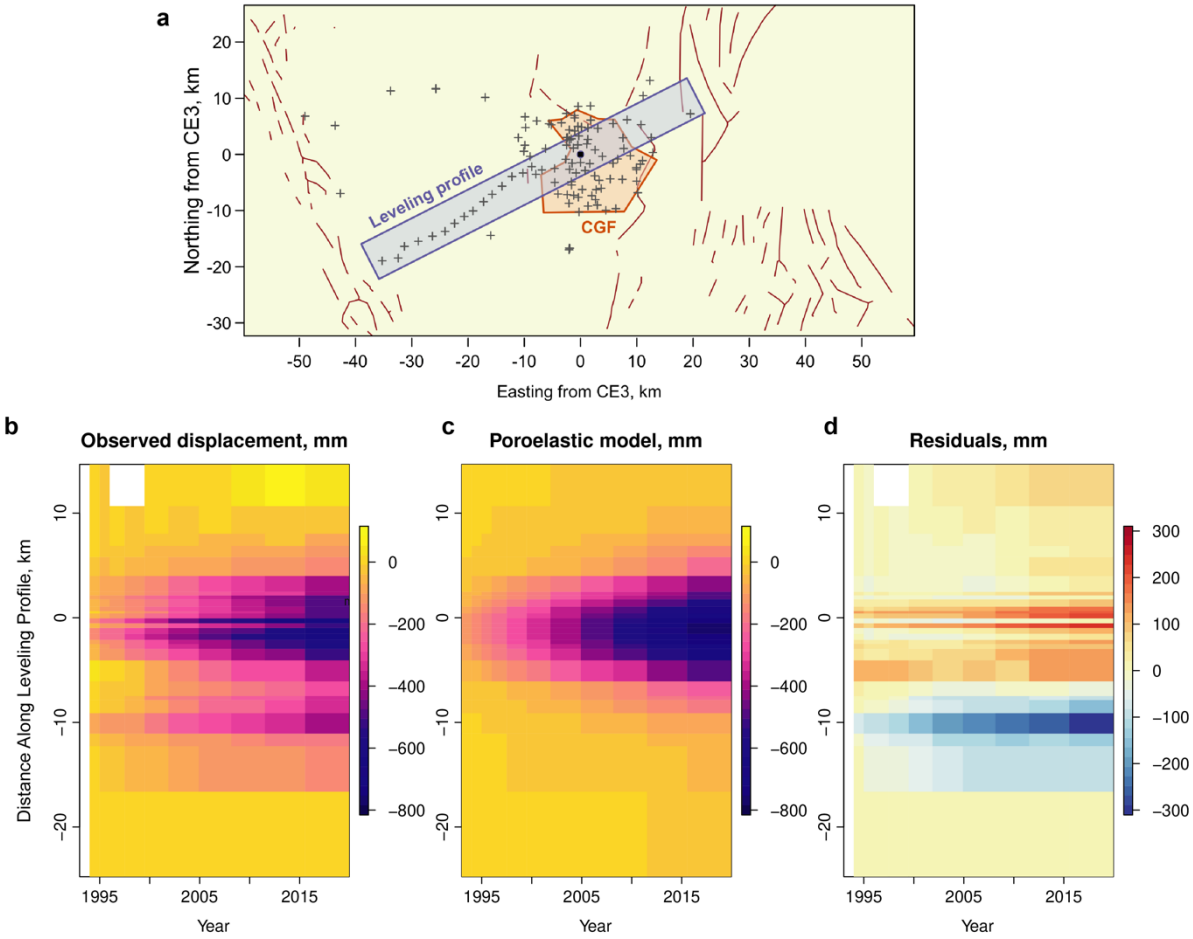

Figure 4: Time-varying deformation and poroelastic model fits at Coso Geothermal Field, adapted from Eneva, et al., (2018). In (a), the orientation of the leveling profile across the CGF. In (b), the observed, relative vertical positions from the leveling data as a function of time. The vertical axis shows distance (in km) along the profile. In (c), the poroelastic model (Segall, 1985) that minimizes misfit for the whole collection of observations. The best-fitting hydraulic diffusivity is ~0.01 m^2/s, which is consistent with inferences from seismic swarms (e.g., Chen, et al., 2012).

2.2 Salton Sea Geothermal Field

The Salton Sea Geothermal Field (SSGF) is the located in the Imperial Valley (IV) in southern California and has been in operation since the early 1980s. Exploration for geothermal energy resources in IV began in the late 1950's, and has continued at a vigorous pace since (Figure 5). At present, industrial geothermal operations have concentrated into four major power plants, of which SSGF produces the majority of energy.

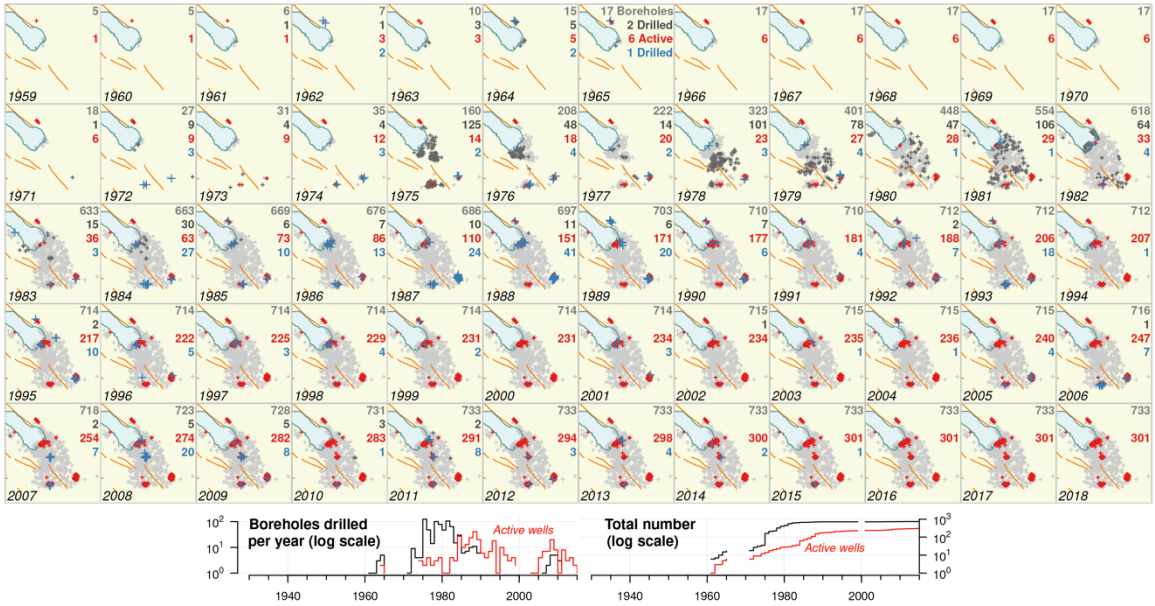

Figure 5: Geothermal exploration and field development in the Imperial Valley, California. Each map shows the number of boreholes drilled in that year, whether for resource assessment or completion as a geothermal well and the total number of boreholes over time. Red and blue + symbols indicate boreholes that were completed as geothermal wells and actively used today, and grey + symbols indicate boreholes that were drilled and only used for exploration (e.g., for temperature profile measurements); the Salton Sea (blue polygon), and major mapped faults (see Figure 1) are shown for reference. The figures on the bottom show timeseries of the number of boreholes drilled per year (left), and the total number of boreholes in existence (right).

Ground deformation in the vicinity of SSGF has been shown to be unmistakably linked to geothermal energy production (Barbour, et al., 2016; Crandall-Bear, et al., 2018), but there is some uncertainty as to the level of natural crustal deformation in the region. Fortuitously, geodetic data were collected prior to the field becoming operational (i.e., Crow and Kasameyer, 1978; Figure 6): these show a clear evolution from surface motion that was most likely related to naturally occurring seismic swarms and perhaps aseismic moment release (e.g., Lohman and McGuire, 2007), to deformation driven by fluid-mass losses.

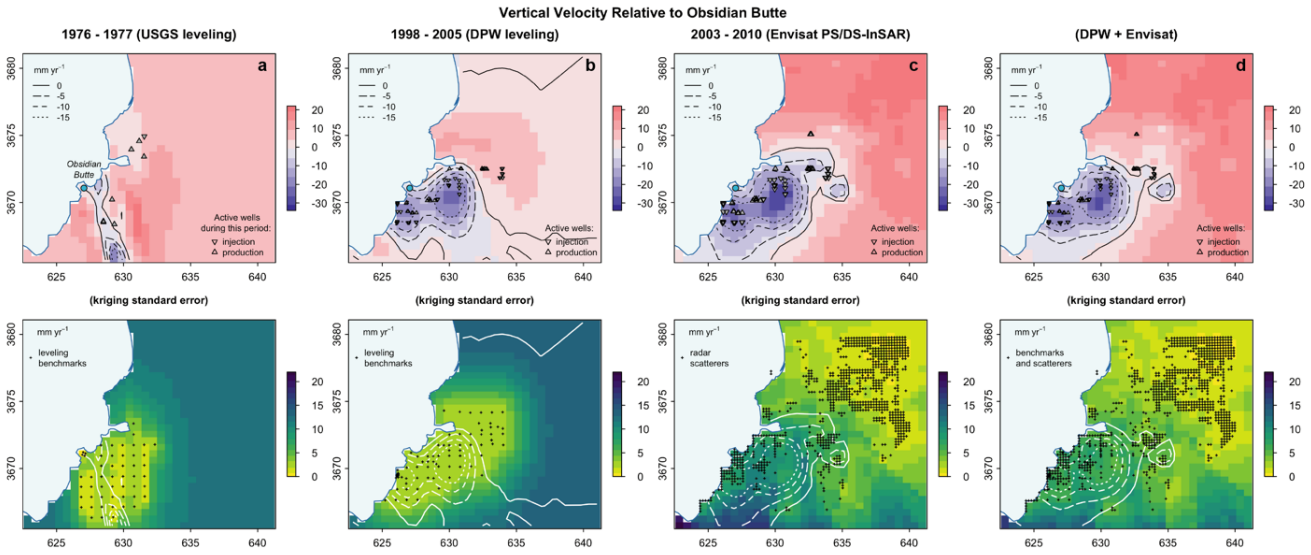

Figure 6: Comparison of vertical ground deformation – rates with respect to Obsidian Butte – at the Salton Sea Geothermal Field. Maps on the top row are vertical rates (in mm/yr; negative values represent subsidence) calculated by applying trans-Gaussian kriging to (a) rates from leveling prior to field expansion (Crow and Kasameyer, 1978), (b) rates estimated from leveling data provided by the Imperial County Department of Public Works ('DPW'; see Acknowledgments), (c) rates estimated from Envisat PS/DS-InSAR (Eneva, et al., 2014; Barbour, et al., 2016), and (d) rates from the combination of the DPW and Envisat datasets. In each frame we show the locations of geothermal injection and production wells that were active during the given time period. Maps on the bottom row show the standard error in the kriging prediction, along with locations of benchmarks and/or scatterers used in InSAR processing.

Although the sources of ground deformation at Salton Sea are well understood as a result of reservoir depletion, the connection between seismicity rates and injection and production is a bit more subtle. The SSGF is located at the Northern end of the Brawley Seismic Zone, a transition zone from the San Andreas fault to the North to the Imperial Fault to the South that shows some the highest rates of seismicity in California. The influence of injection and production of geothermal fluids is apparent when total volumes across the field are calculated and compared to seismicity rates; these show evidence of swarm-like behavior by comparison to Episodic Type Aftershock Sequence (ETAS) models of time-varying earthquake nucleation rates (Brodsky and Lajoie, 2013; Llenos and Michael, 2016). This appears to be a common observation among geothermal fields in California (i.e., Trugman, et al., 2016), which suggests that our understanding of natural seismic hazard in these regions may be biased.

2.3 North Brawley Geothermal Field

The North Brawley Geothermal Field (NBGF) has been in operation in two distinct phases: the first from early 1982 through late 1985; the second from early 2009 through the present. The largest induced earthquake sequence in a geothermal setting occurred in 2012, with a mainshock magnitude of **M**5.4 (Figure 7). Details surrounding this event show evidence for thermal effects and aseismic deformation (Wei, et al., 2015), and InSAR and GPS data (Hauksson, et al., 2013; Eneva, et al., 2019b) capture triggered transient deformation associated with the sequence.

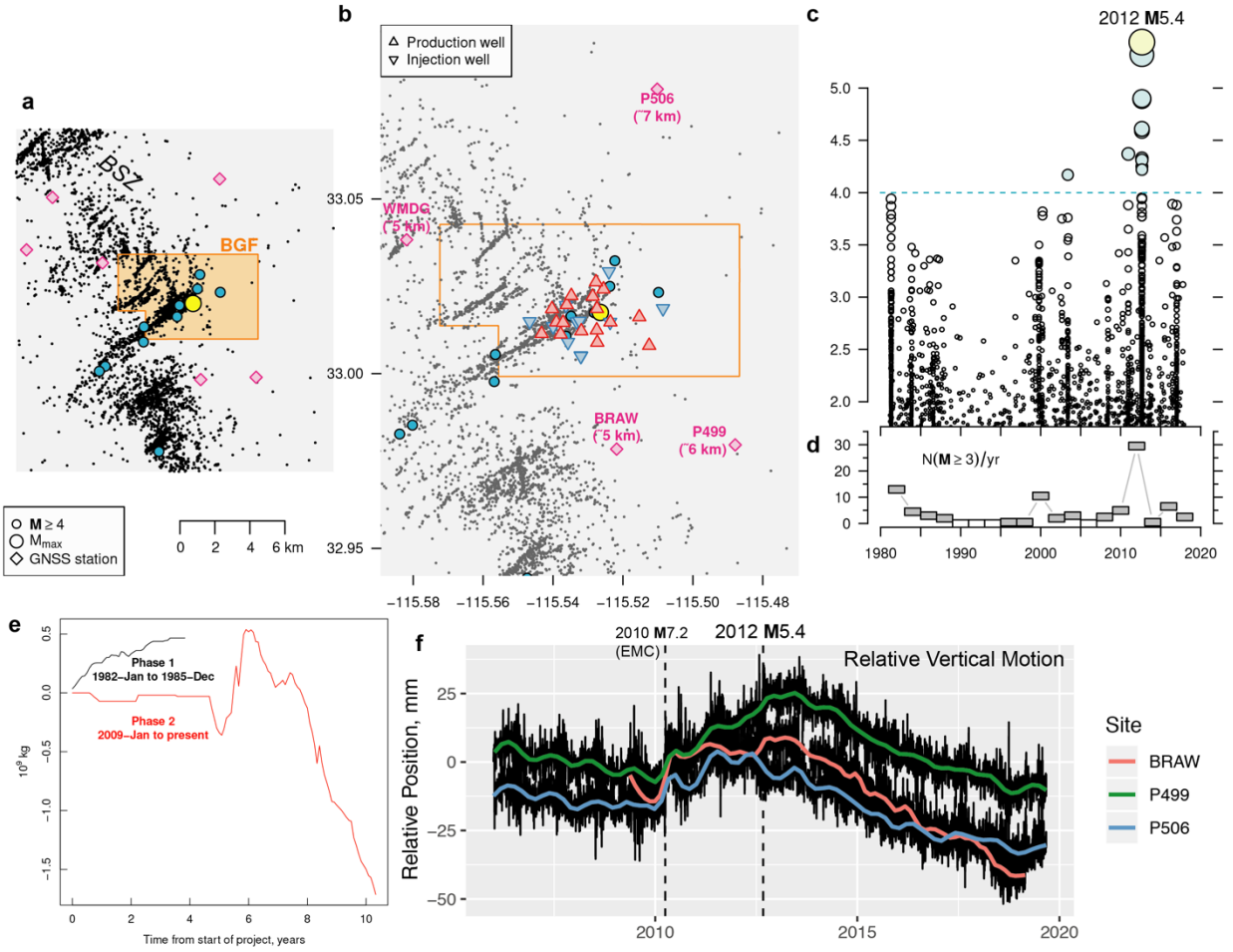

Figure 7: Seismicity and deformation at the North Brawley Geothermal Field (NBGF). (a) Regional seismicity in the Brawley Seismic Zone (BSZ), with locations of M>=4 earthquakes and continuous GNSS stations (diamonds). (b) Zoom in on NBGF wells and associated seismicity. The 2012 M5.4 epicenter is the large circle around the centroid of the geothermal wells. (c) Time evolution of seismicity magnitudes, showing the M5.4 sequence. (d) Rates of M≧3 seismicity in two-year intervals (unfilled boxes indicate no earthquakes). (e) Cumulative net produced fluid (positive indicates fluid-mass loss). These curves should be zero, or very nearly zero because this field uses binary technology; however, in the last five years more fluid has been injected than produced. (f) GPS observations of transient, vertical ground deformation associated with the 2010 M7.2 El Mayor Cucapah earthquake in Mexico, followed by deformation associated with the 2012 M5.4 Brawley earthquake sequence (see Hauksson, et al., 2013). Solid lines show local regression smoothing applied to daily relative positions (in mm).

2.4 Heber Geothermal Field

The Heber Geothermal Field (HGF) has utilized both dual-flash and binary power generation technology since 1985 and 1993, respectively, to produce around 90 MWe. The aggregate reinjection history shows low levels of fluid-mass loss, which suggests that little deformation may be expected from reservoir depletion; however, geodetic data from InSAR capture long-term, localized surface deformation, with subsidence rates in excess of 20 mm/yr (Eneva, et al., 2013, 2019a). The HGF field lies approximately 10-20 km West of the Imperial Fault (Figure 9a), a major plate-boundary fault that has generated large-magnitude earthquakes within the last

century. Recently Eneva, et al., (2019a) show data from a dense leveling survey collected at HGF annually since ~1994 (Figure 9b). These geodetic data capture a nearly decade-long deformation transient that initiates between 2004 and 2005, at the time of major changes in fluid injection and production rates, ending in 2015 (Figure 9c-d). The spatial pattern (Figure 9e) confirms that Envisat-based InSAR results represent measurements of this transient as well.

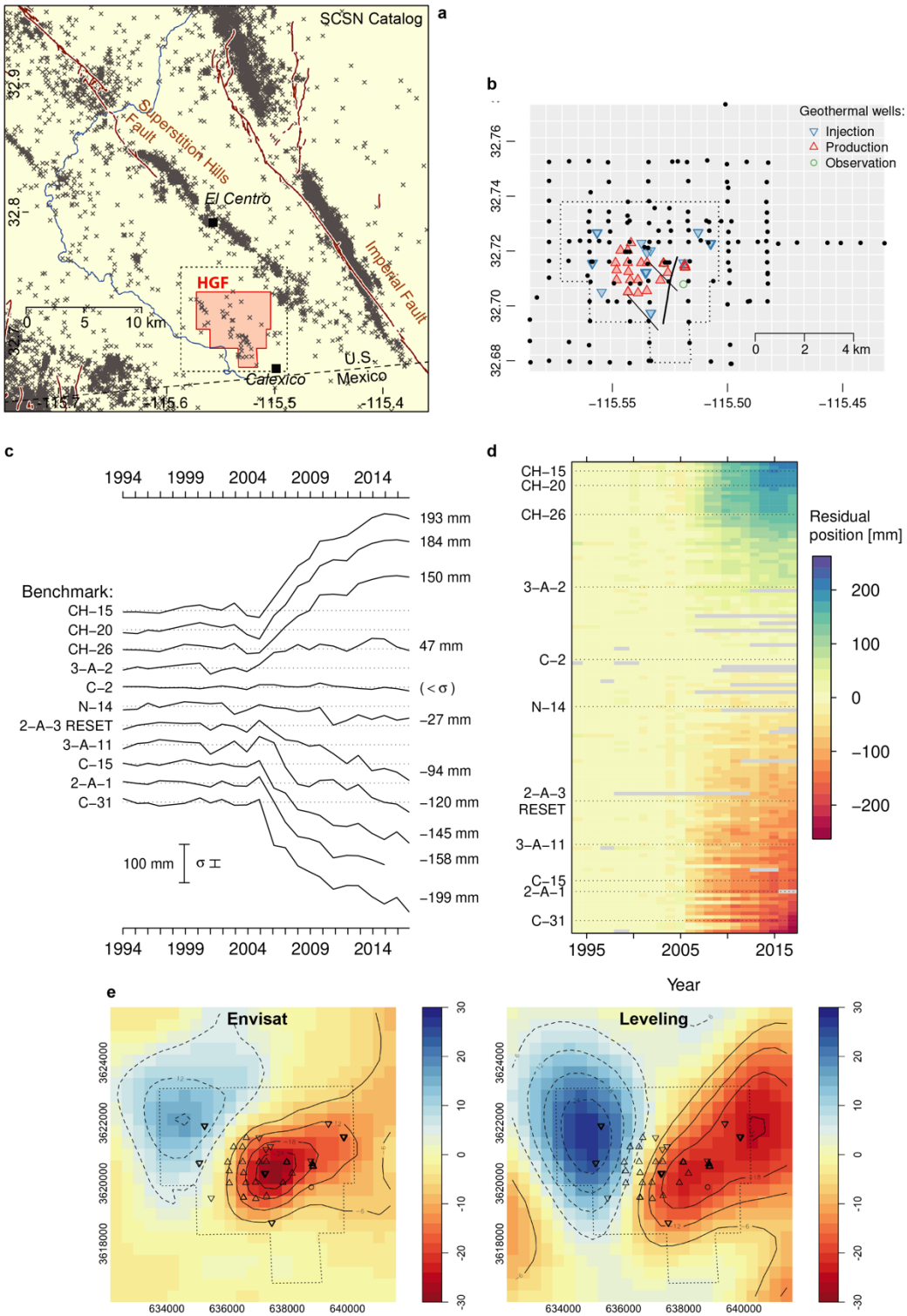

Figure 8: Slow, transient deformation at the Heber Geothermal Field (HGF). (a) Regional map of seismicity, major plate-boundary fault, and boundaries of the HGF. (b) Local map of leveling benchmarks and geothermal wells at HGF. Lines mark known, reservoir-bounding faults from active-source seismic data and borehole spinner and temperature logs (e.g. James, et al., 1987). (c) Selected timeseries of leveling positions (e.g., Eneva, et al., 2019a) after subtracting a constant trend determined from data prior to 2005. (c) Timeseries from all benchmarks as an image, with colors representing relative vertical motion. (e) Comparison of vertical rates (in mm/yr; negative values represent subsidence) from Envisat InSAR (left, from Eneva, et al., 2013) and rates derived from transient displacement in leveling data (right) from 2005 through 2018.

Low levels of seismicity at HGF were first detected around 1993, but enough events have been detected by the regional seismic network – the Southern California Seismic Network – that a series of rapid increases in seismicity rate have been observed from the initiation of the transient deformation in 2004 through 2007 on structures flanking the geothermal wells (Figure 9). Barbour, et al. (2019) used a match-filter detection algorithm to improve and enhance that catalog. This yields a nearly tenfold increase in detected events, with similar temporal patterns (Figure 9c).

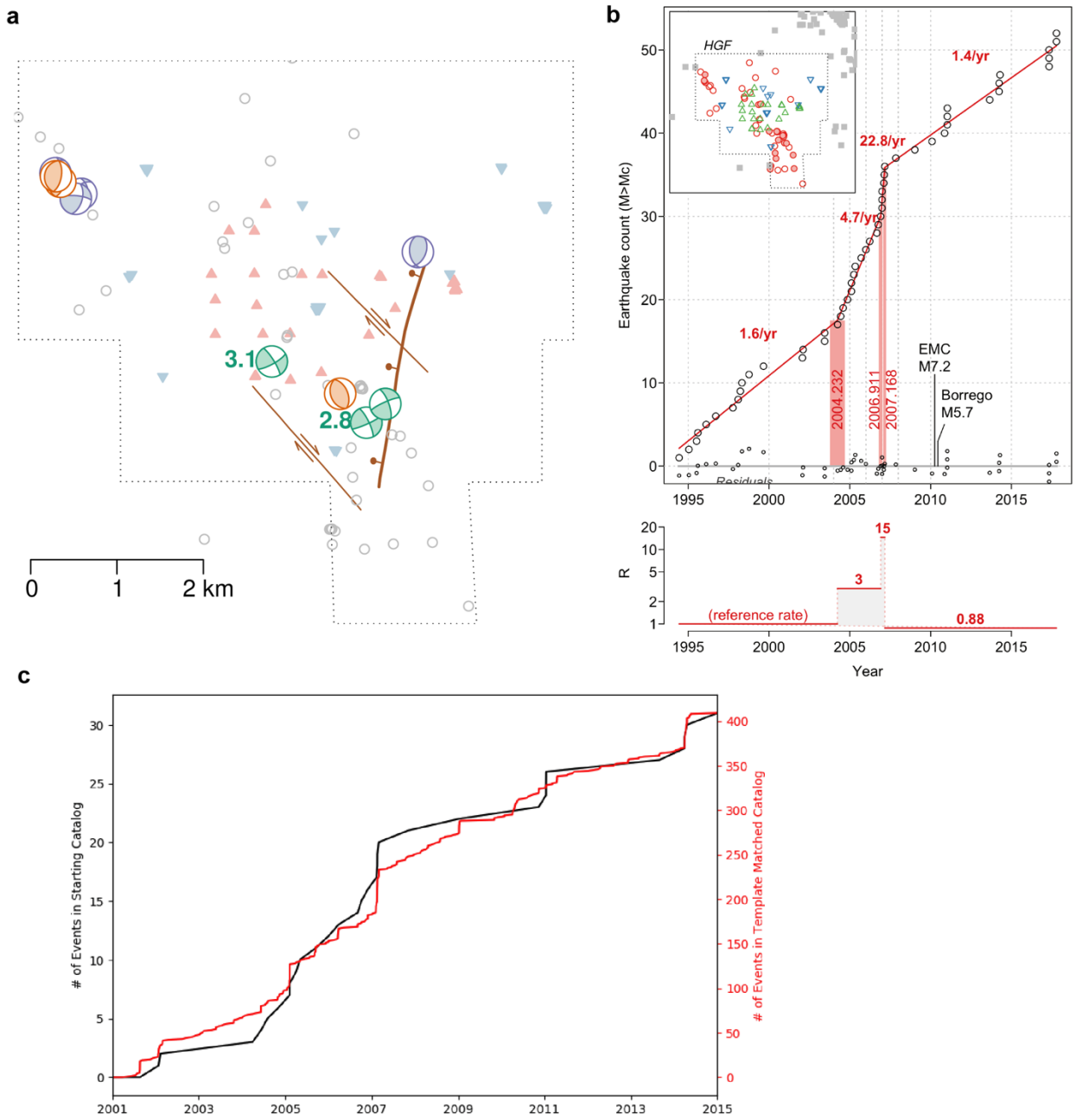

Figure 9: Rapid seismicity rate changes at the Heber Geothermal Field (HGF). (a) Map of seismicity with focal mechanisms, reservoir bounding faults, and geothermal wells in the HGF. (b) Cumulative seismicity within the HGF boundary. The vertical red bars mark times of significant rate changes – late 2005, late 2006, early 2007 – with their relative rate shown below. (c) Comparison of the original seismic catalog and the improved catalog from template matching (from Barbour, et al., 2019).

In consideration of both geodetic and seismic observations at HGF, we find that changes in seismicity rate are nearly instantaneous and correspond to significant changes in injection and production; whereas, ground deformation occurs slowly. This suggests that reservoir bounding faults are critically loaded and thus small perturbations in stressing rates may induced brittle failure (earthquakes). In contrast, the slow deformation opens up the possibility that the physical mechanisms responsible for these signals include triggered slow slip on reservoir bounding faults (e.g., Lohman and McGuire, 2007; Helmstetter and Shaw, 2009; Guglielmi, et al., 2015), including a previously imaged "feeder fault" (the normal fault seen in Figure 9a), and a poroelastic step-response (e.g., Rudnicki, 1986) to systematic changes in fluid injection and production reported at the field (Figure 10).

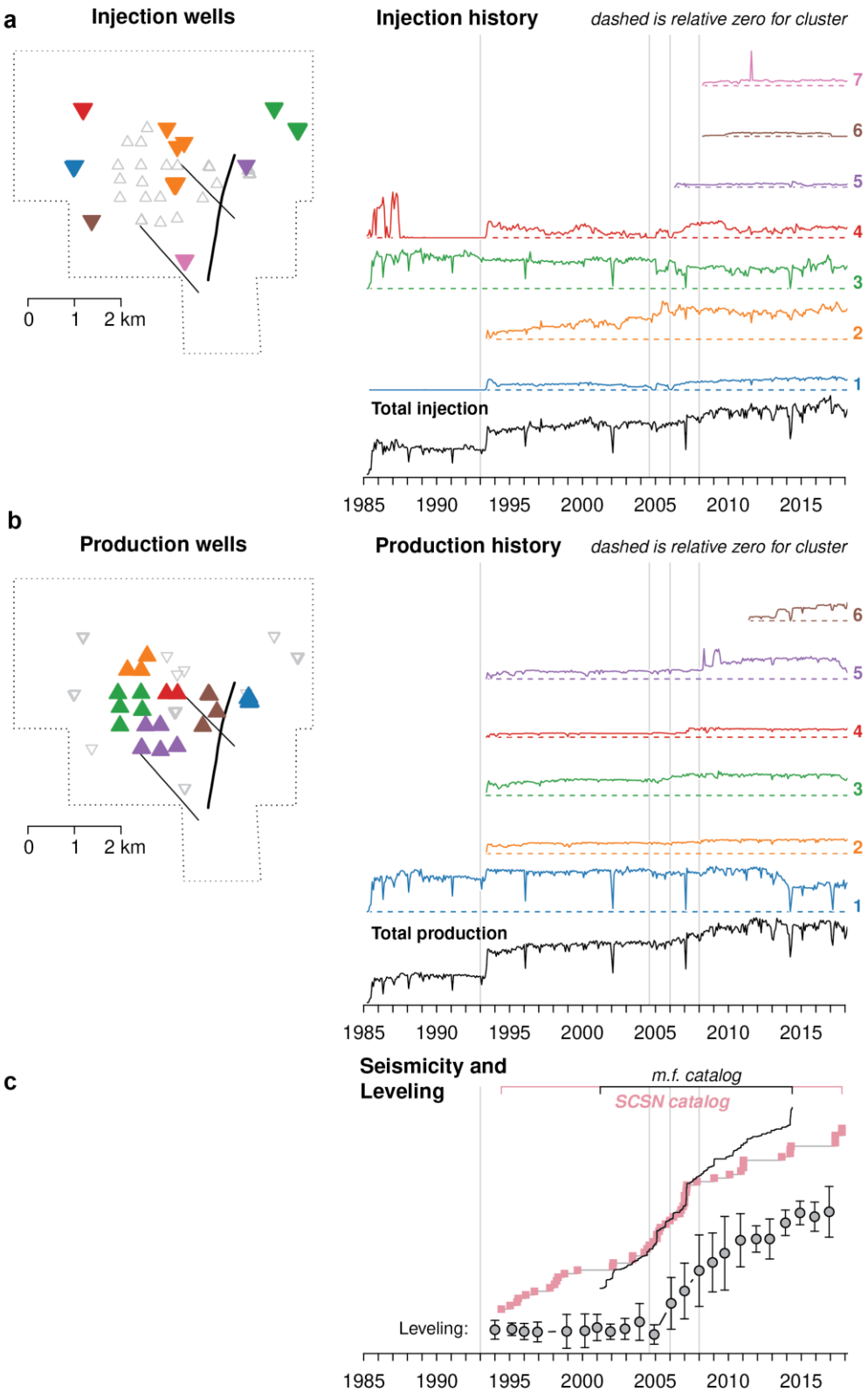

Figure 10: Injection (a) and production (b) records at HGF, compared to (c) seismicity rates and transient deformation measured by a dense leveling network. In (a) and (b), wells are grouped into spatial clusters (see maps on left) and the corresponding timeseries for total volumes in each cluster are shown to the right. Additionally, the total injection and production records are shown at the bottom, respectively. Vertical lines are times of new power plants coming online. In (c) an earthquake catalog obtained by matched-filter detection is compared to the starting SCSN catalog (from Barbour, et al., 2019), and to characteristic leveling motions (amplitudes divided by their root-mean-square value) across the array of benchmarks.

3. CONCLUSION

Decades of seismic and geodetic data from geothermal fields in southern California reveal two of the predominant seismic and geologic risks associated with geothermal energy production: long-term subsidence and induced seismicity. Recent technological advancements in processing of these data illuminate an additional time-varying component of these hazards. Four major geothermal fields in southern California exhibit different time histories of injection and production activities and different physical responses in terms of seismicity and ground deformation. Comparing these observations highlight the inherent feedback between the dominant modes of moment release, permeability, and structural complexity. At the same time these observations suggest a non-stationary seismic hazard potential in critical areas like plate-boundary transition zones, with possible anthropogenic influences. Modeling the specific feedbacks that drive this deformation is an important target for further understanding time-dependent seismic hazard and its relation to energy production in large geothermal areas.

ACKNOWLEDGMENTS

Injection and production volumes were obtained from the California Department of Conservation Division of Oil, Gas, and Geothermal Resources (https://www.conservation.ca.gov/dog). Leveling data for Salton Sea and Heber geothermal fields were obtained from the Imperial County Dept. of Public Works (https://www.co.imperial.ca.us). Seismic data are from the Southern California Seismic Network (DOI: 10.7914/SN/CI), specifically the relocated catalog (https://scedc.caltech.edu/research-tools/alt-2011-dd-hauksson-yang-shearer.html). (Websites last accessed October 2019.) This work was supported by the California Energy Commission (grant # GEO-16-003 awarded to Imageair Inc.); most of the geodetic data shown here are also from this project, with InSAR processing provided by TRE Altamira Inc., and I thank Mariana Eneva for help preparing and accessing these data. I thank Mariana Eneva, Kathryn Materna, and Elizabeth Cochran for insightful comments that improved this paper. Any use of trade, firm, or product names is for descriptive purposes only and does not imply endorsement by the U.S. Government.

REFERENCES

Ali, S. et al. (2016), Time-series analysis of surface deformation at Brady Hot Springs geothermal field (Nevada) using interferometric synthetic aperture radar, Geothermics, 61, 114 – 120, DOI: 10.1016/j.geothermics.2016.01.008

Axelsson, G. (2012), The Physics of Geothermal Energy. In Sayigh, A. (ed.) Comprehensive Renewable Energy, 7.02, 3 – 50, Elsevier, Oxford, DOI:10.1016/B978-0-08-087872-0.00703-4

Barbour, A. J., Skoumal, R., and A. Crandall-Bear (2019), Slow Deformation and Rapid Seismicity-Rate Changes Triggered by Geothermal Fluid Redistribution, Proceedings of the Third Schatzalp Workshop on Induced Seismicity, Davos, Switzerland, 5-8 Match, available online at http://www.seismo.ethz.ch/en/research-and-teaching/schatzalp-workshop/download-2019/ (last accessed Oct 2019)

Barbour, A. J., Evans, E. L., Hickman, S. H. & Eneva, M. (2016), Subsidence Rates at the Southern Salton Sea Consistent with Reservoir Depletion. J. Geophys. Res. Solid Earth, 121, 5308–5327, DOI: 10.1002/2016JB012903

Brodsky, E. E., and L. J. Lajoie (2013), Anthropogenic seismicity rates and operational parameters at the Salton Sea geothermal field, Science, 341(6145), 543–546, doi:10.1126/science.1239213

California Energy Commission (CEC) (2019), Power Plant Owner Reporting Database, Technical Report, QFER CEC-1304, available online at https://ww2.energy.ca.gov/almanac/electricity_data/web_qfer/index_cms.php (last accessed Oct 2019)

Chen, X., Shearer, P.M., and Abercrombie, R.E. (2012), Spatial Migration of Earthquakes Within Seismic Clusters in Southern California: Evidence for Fluid Diffusion, J. Geophys. Res., 117(B4), doi: 10.1029/2011JB008973.

Crandall-Bear, A. T., A. J. Barbour, and M. Schoenball (2018), Irregular Focal Mechanisms Observed at Salton Sea Geothermal Field: Possible Influences of Anthropogenic Stress Perturbations, Proceedings of the 43rd Workshop on Geothermal Reservoir Engineering, SGP-TR-213, Stanford University, Stanford, California, 12-14 Feb.

Crow, N. B., and P. W. Kasamayer (1978), Monitoring natural subsidence and seismicity in the Imperial Valley as a basis for evaluating potential impacts of geothermal production, Geotherm. Resour. Council Trans., *2*, 125–128.

Eneva, M., Adams, D., Falorni, G. & Morgan, J. (2013), Application of Radar Interferometry to Detect Subsidence and Uplift at the Heber Geothermal Field, Southern California, Geotherm. Resour. Council Trans., 37, 491–499

Eneva, M., D. Adams, G. Falorni, F. Novali, and V. Hsiao (2014), Surface deformation at the Salton Sea geothermal field from high-precision radar interferometry, Geotherm. Resour. Council Trans., 38, 991–999.

Eneva, M., Barbour, A. J., Adams, D., Hsiao, V., Blake, K., Falorni, F., and R. Locatelli (2018), Satellite Observations of Surface Deformation at the Coso Geothermal Field, California, Geotherm. Resour. Council Trans., 42, 1383-1401

Eneva, M., Adams, D., Hsiao, V., Falorni, G. & Locatelli, R. (2019a), Surface Deformation at the Heber Geothermal Field in Southern California. In Proceedings of the 44th Workshop on Geothermal Reservoir Engineering, SGP-TR-214. Stanford University, Stanford, California, February 11-13

Eneva, M., D. Adams, G. Falorni, and M. Shumski (2019b), Surface deformation and seismicity at the North Brawley geothermal field in southern California, Geotherm. Resour. Council Trans., 43.

Fialko, Y. and Simons, M. (2000), Deformation and seismicity in the Coso geothermal area, Inyo County, California: Observations and modeling using satellite radar interferometry, J. Geophys. Res. Solid Earth, 105, 21781–21793, DOI: 10.1029/2000JB900169

Guglielmi, Y., Cappa, F., Avouac, J.-P., Henry, P. and Elsworth, D. (2015), Seismicity triggered by fluid injection–induced aseismic slip, Science, 348, 1224–1226, DOI: 10.1126/science.aab0476

Hauksson, E., Yang, W. & Shearer, P. M. (2012), Waveform Relocated Earthquake Catalog for Southern California (1981 to June 2011), Bull. Seismol. Soc. Am., 102, 2239–2244, DOI: 10.1785/0120120010

Hauksson, E., Stock, J.M., Bilham, R., Boese, M., Chen, X., Fielding, E.J., Galetzka, J.E., Hudnut, K.W., Hutton, K., Jones, L.M., Kanamori, H., Shearer, P.M., Steidl, J.H., Treiman, J.A., Wei, S., and Yang, W (2013), Report on the August 2012 Brawley Earthquake Swarm in Imperial Valley, Southern California, Seismological Research Letters, 84(2), 177-189, DOI: 10.1785/0220120169

Helmstetter, A. and Shaw, B. E. (2009), Afterslip and aftershocks in the rate-and-state friction law, J. Geophys. Res. Solid Earth, 114, DOI: 10.1029/2007JB005077

James, E.D., Hoang, V.T., and Epperson, I.J. (1987), Structure, permeability and production characteristics of the Heber, California geothermal field: Proceedings, 12th Workshop on Geothermal Reservoir Engineering, Stanford University, p. 267-271.

Kaven, J.O., Hickman, S.H., and Davatzes, N.C (2015), Seismicity and Deformation in the Coso Geothermal Field from 2000 to 2012, Geophys. Res. Abstracts, 17, EGU2015-14466.

Llenos, A. L., and A. J. Michael (2016), Characterizing potentially induced earthquake rate changes in the Brawley Seismic Zone, Southern California, Bull. Seismol. Soc. Am., 106 (5): 2045-2062, DOI: 10.1785/0120150053

Lohman, R. B., and J. J. McGuire (2007), Earthquake swarms driven by aseismic creep in the Salton Trough, California, J. Geophys. Res., *112*, B04405, doi:10.1029/2006JB004596

Majer, E. L., and Peterson, J. E. (2007). The impact of injection on seismicity at The Geysers, California Geothermal Field. International Journal of Rock Mechanics and Mining Sciences, 44(8), 1079-1090, DOI: 10.1016/j.ijrmms.2007.07.023

Martínez-Garzón, P., Kwiatek, G., Bohnhoff, M., and Dresen, G. (2016), Impact of fluid injection on fracture reactivation at The Geysers geothermal field, J. Geophys. Res. Solid Earth, 121, 7432– 7449, doi:10.1002/2016JB013137.

Mossop, A. and Segall, P. (1997), Subsidence at The Geysers Geothermal Field, N. California from a comparison of GPS and leveling surveys. Geophys. Res. Lett., 24, 1839–1842, DOI: 10.1029/97GL51792

Rudnicki, J. W. (1986), Fluid mass sources and point forces in linear elastic diffusive solids. Mech. Mater., 5, 383–393, DOI:10.1016/0167-6636(86)90042-6

Segall, P (1985), Stress and Subsidence Resulting from Subsurface Fluid Withdrawal in the Epicentral Region of the 1983 Coalinga Earthquake, J. Geophys. Res., 90(B8), (1985), 6801–6816, doi: 10.1029/JB090iB08p06801.

Segall, P. and Fitzgerald, S. D. (1998), A note on induced stress changes in hydrocarbon and geothermal reservoirs. Tectonophysics, 289, 117–128, DOI: 10.1016/S0040-1951(97)00311-9

Trugman, D. T., Shearer, P. M., Borsa, A. A., and Fialko, Y. (2016), A comparison of long‐term changes in seismicity at The Geysers, Salton Sea, and Coso geothermal fields, J. Geophys. Res. Solid Earth, 121, 225– 247, DOI: 10.1002/2015JB012510

Vasco, D.W., Wicks, C., Karasaki, K., and Marques, O. (2002), Geodetic Imaging: Reservoir Monitoring Using Satellite Interferometry, Geophys. J. Int., 149, 555-571.

Wei, S., Avouac, J. P., Hudnut, K. W., Donnellan, A., Parker, J. W., Graves, R. W., ... & Eneva, M. (2015). The 2012 Brawley swarm triggered by injection-induced aseismic slip. Earth and Planetary Science Letters, 422, 115-125, DOI: 10.1016/j.epsl.2015.03.054

Wicks, C., Tatcher, W., Monastero, F., and Hasting, M. (2001), Steady-State Deformation of the Coso Range, East Central California, Inferred from Satellite Radar Interferometry, J. Geophys. Res., 106, 13769-13780.